Supplementary Materials

Efficient solar-driven interfacial steam-hydropower co-generation by high-quality carbon nanotube from discarded polyolefin separator

Huiyue Wang, Mengjie Xu, Xueying Wen, Guixin Hu, Qianyu Wei, Lingling Feng, Xinyao Zhang, Ran Niu, Jiang Gong*

Key Laboratory of Material Chemistry for Energy Conversion and Storage, Ministry of Education, Hubei Key Laboratory of Material Chemistry and Service Failure, School of Chemistry and Chemical Engineering, Huazhong University of Science and Technology, Wuhan 430074, Hubei, China.

Correspondence to: Prof. Jiang Gong, Key Laboratory of Material Chemistry for Energy Conversion and Storage, Ministry of Education, Hubei Key Laboratory of Material Chemistry and Service Failure, School of Chemistry and Chemical Engineering, Huazhong University of Science and Technology, Wuhan 430074, Hubei, China. E-mail: gongjiang@hust.edu.cn

Supplementary Figure 1. Photographs of discarded PE separators.

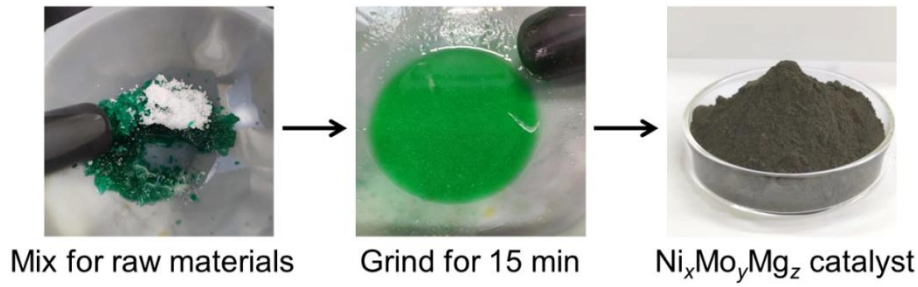

Supplementary Figure 2. The preparation process of $Ni_xMo_yMg_z$ catalyst.

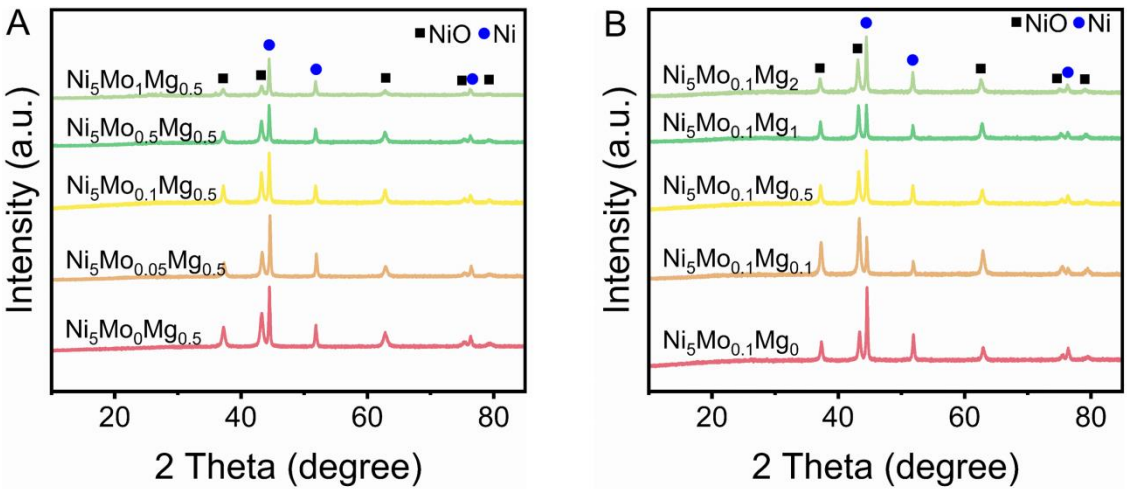

Supplementary Figure 3. XRD patterns of (A) $Ni_5Mo_yMg_{0.5}$ and (B) $Ni_5Mo_{0.1}Mg_z$.

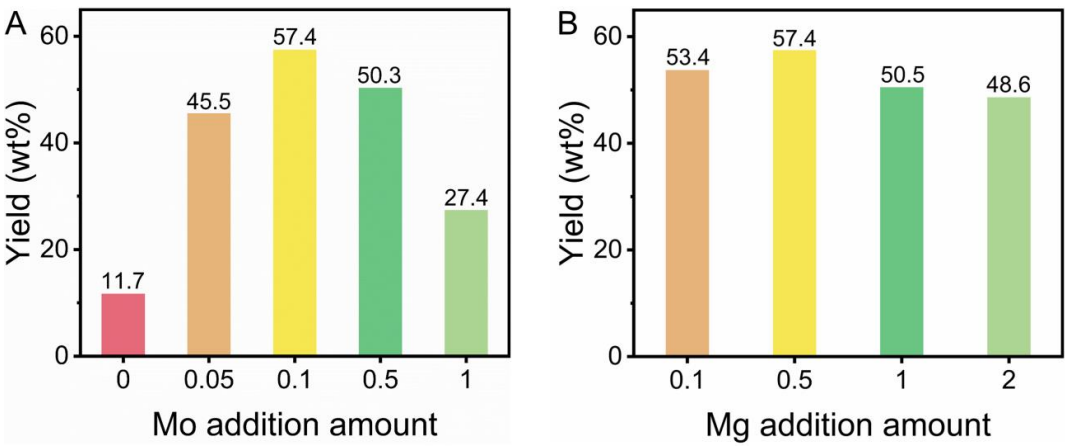

Supplementary Figure 4. The yield of $CNT_{x\text{-}y\text{-}z}$ using (A) $Ni_5Mo_yMg_{0.5}$ and (B) $Ni_5Mo_{0.1}Mg_z$.

Note: When $Ni_5Mo_{0.1}Mg_0$ is used as the catalyst, the product is aggregated spherical carbon particles with the size of 50–200 nm, rather than CNTs. The yield of spherical carbon particles is calculated to be 16.5 wt%.

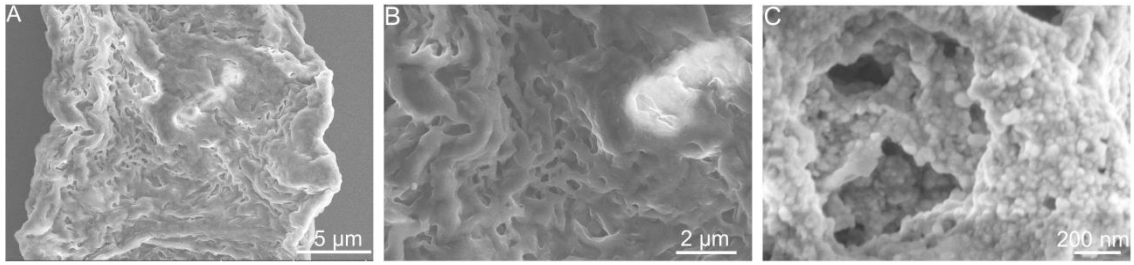

Supplementary Figure 5. (A-C) SEM images of $Ni_5Mo_{0.1}Mg_{0.5}$ catalyst.

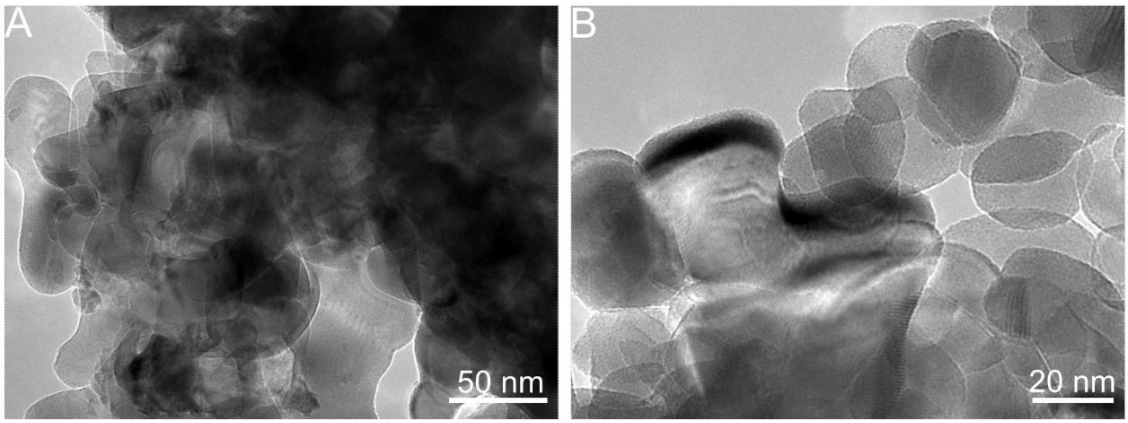

Supplementary Figure 6. (A and B) TEM images of $Ni_5Mo_{0.1}Mg_{0.5}$ catalyst.

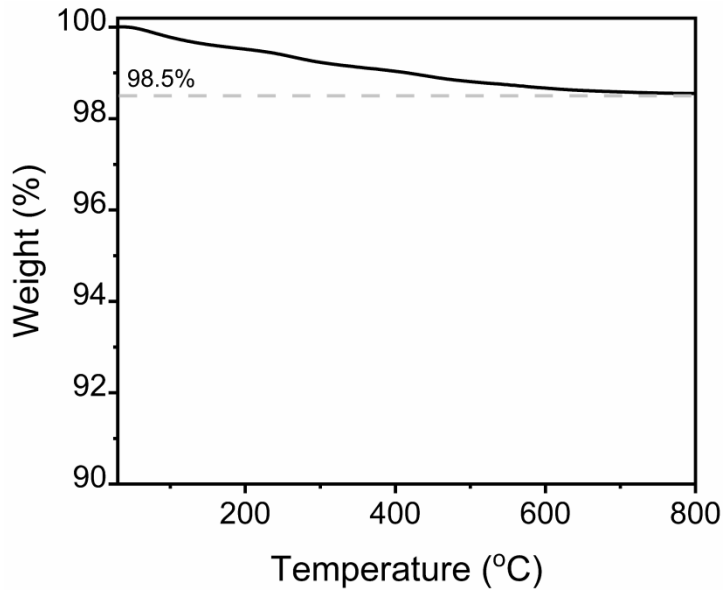

Supplementary Figure 7. TGA curve of $Ni_5Mo_{0.1}Mg_{0.5}$ catalyst.

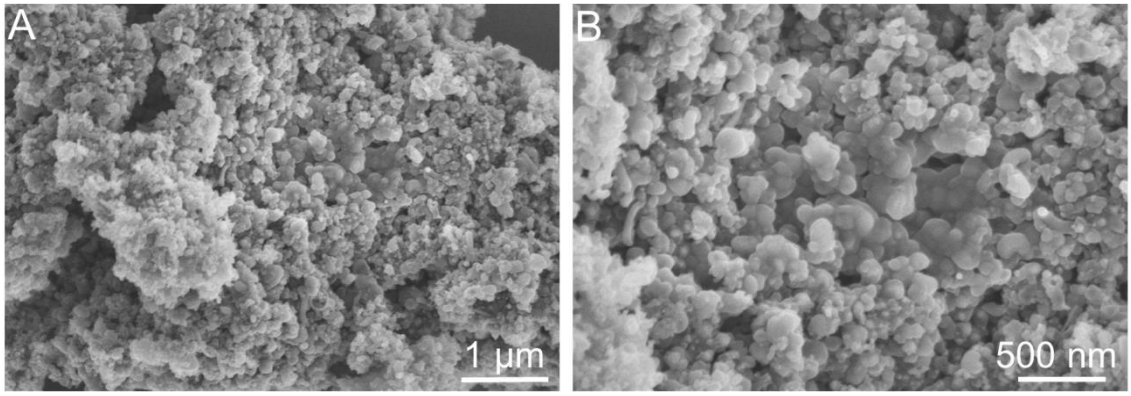

Supplementary Figure 8. (A and B) SEM images of $OCNT_{5\text{-}0.1\text{-}0}$.

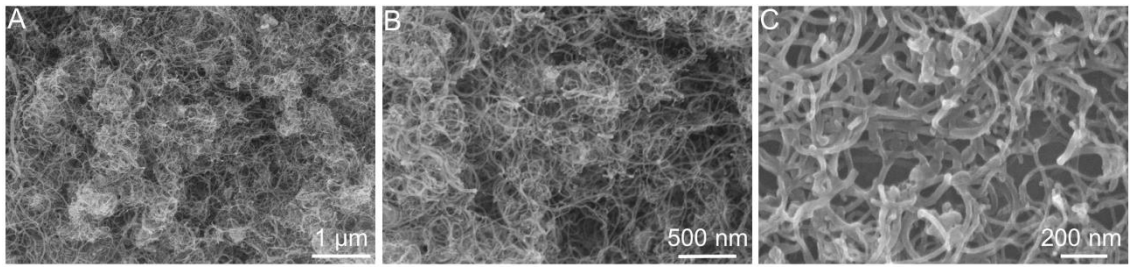

Supplementary Figure 9. (A-C) SEM images of $OCNT_{5\text{-}0.1\text{-}2}$.

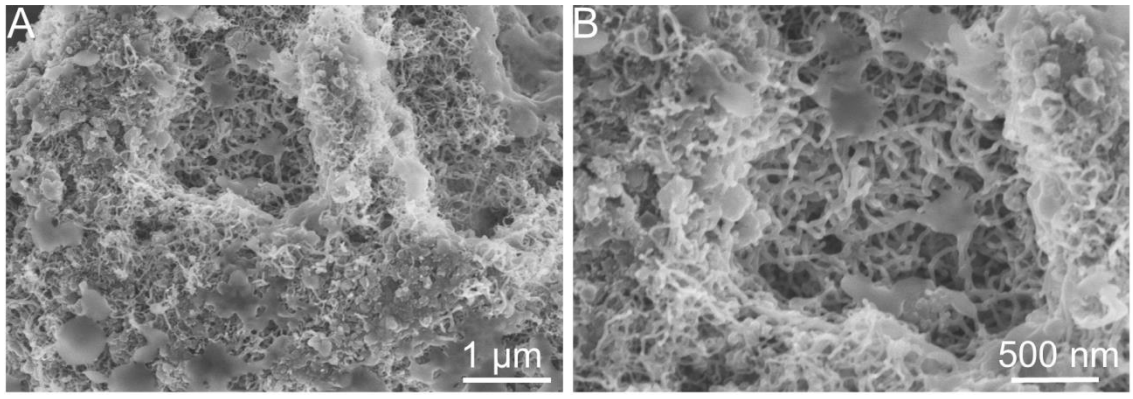

Supplementary Figure 10. (A and B) SEM images of $OCNT_{5\text{-}0\text{-}0.5}$.

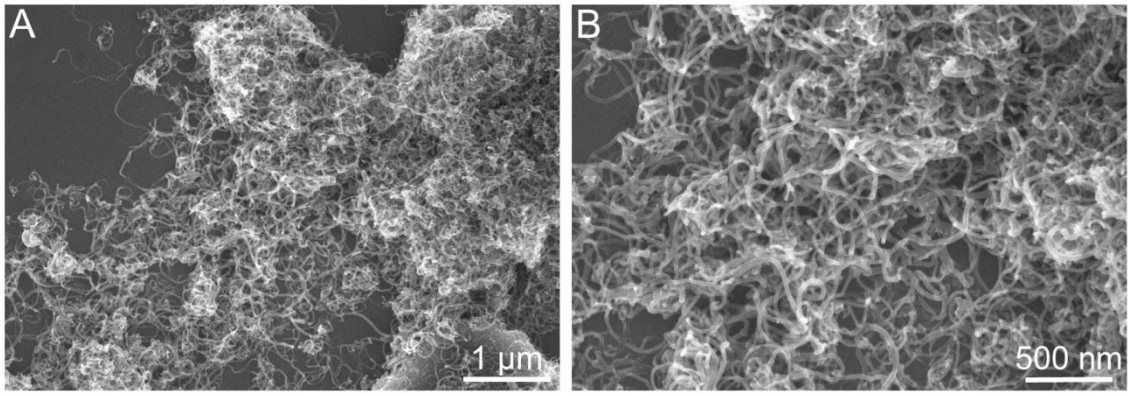

Supplementary Figure 11. (A and B) SEM images of $OCNT_{5\text{-}0.1\text{-}0.5}$.

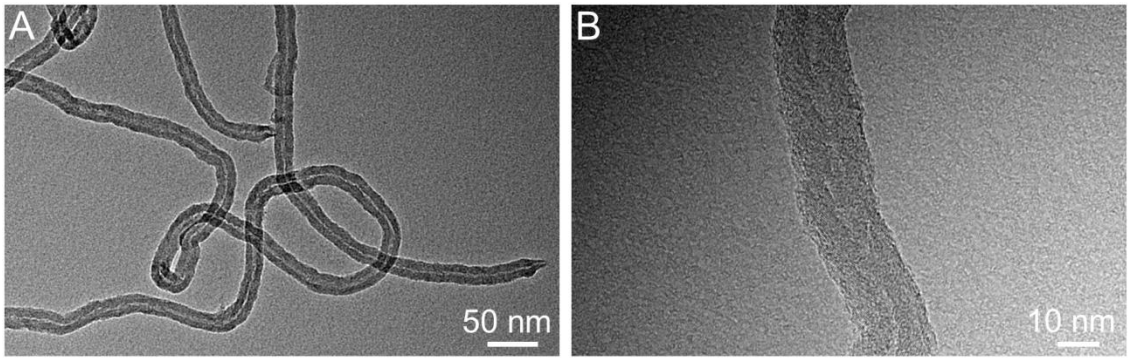

Supplementary Figure 12. (A and B) TEM images of $OCNT_{5\text{-}0.1\text{-}0.5}$.

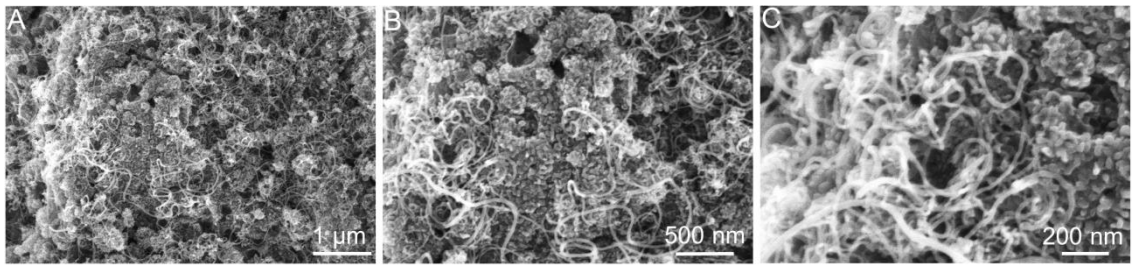

Supplementary Figure 13. (A-C) SEM images of $OCNT_{5\text{-}1\text{-}0.5}$.

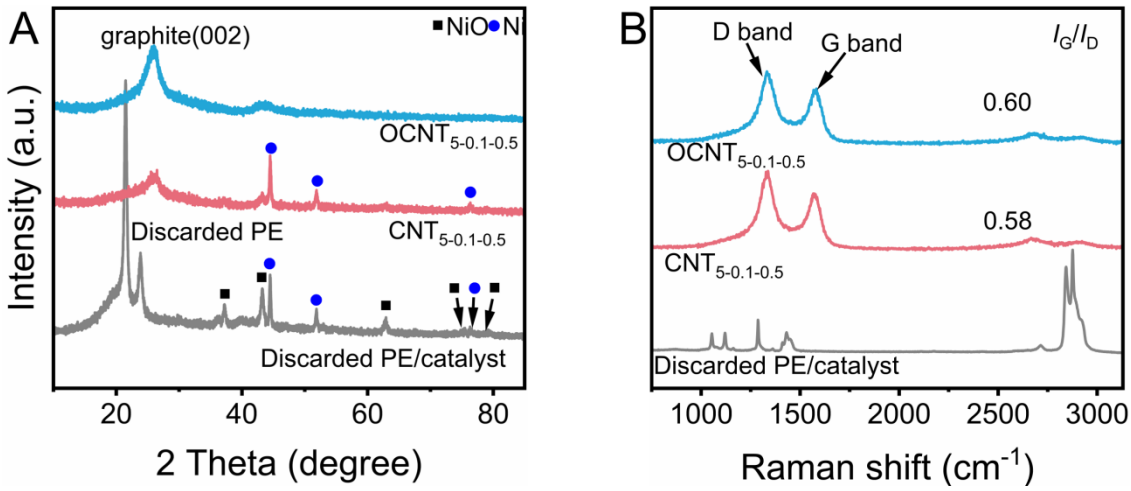

Supplementary Figure 14. (A) XRD patterns and (B) Raman spectra of $OCNT_{5\text{-}0.1\text{-}0.5}$, $CNT_{5\text{-}0.1\text{-}0.5}$ and discarded PE/catalyst.

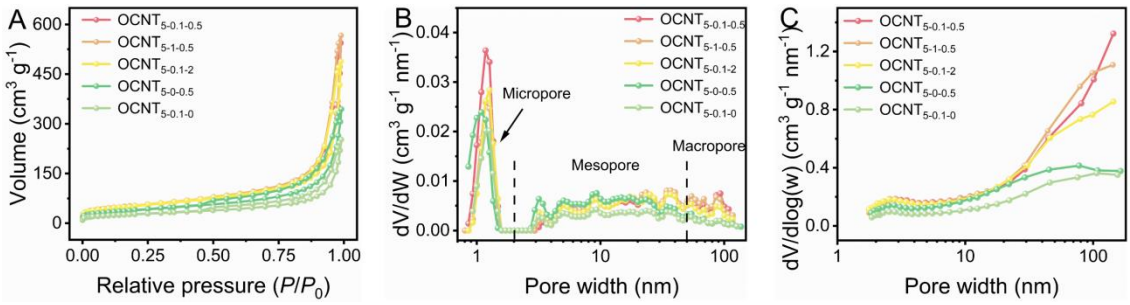

Supplementary Figure 15. (A) N_2 adsorption-desorption isotherms and pore size distribution plots using (B) DFT or (C) BJH model of $OCNT_{x\text{-}y\text{-}z}$.

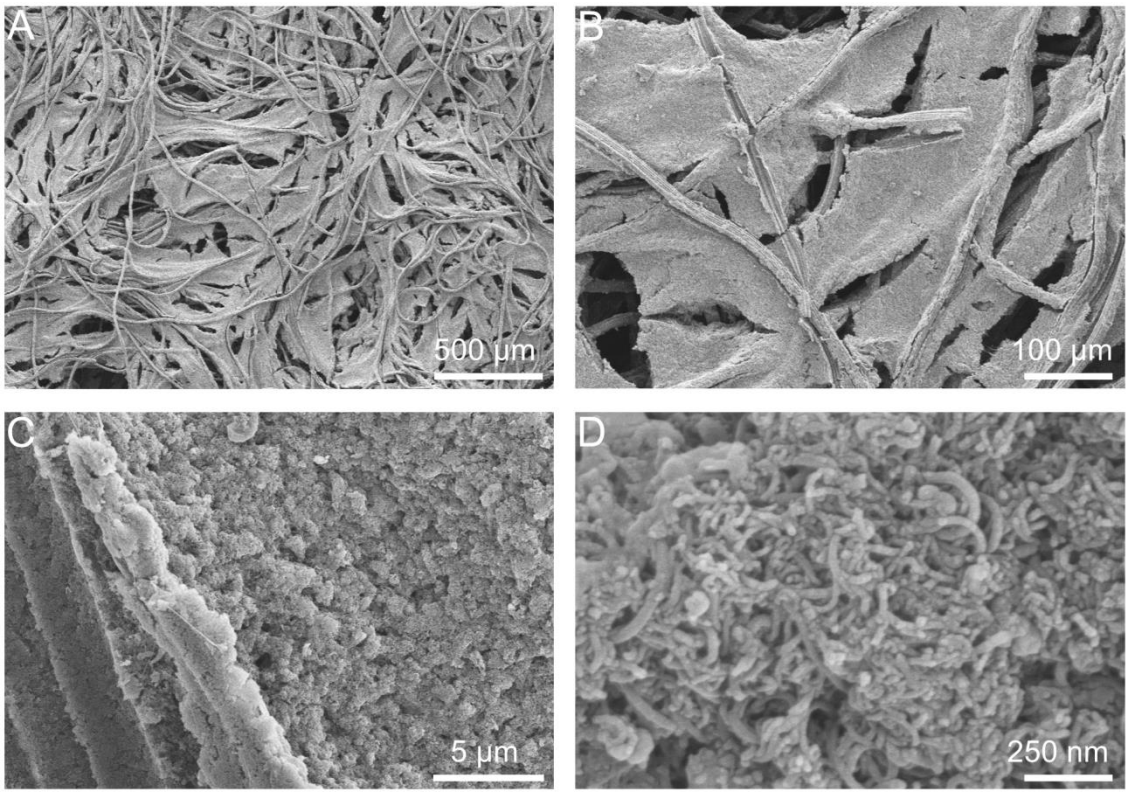

Supplementary Figure 16. (A-D) SEM images of $OCNT_{5\text{-}0.1\text{-}0.5}$ evaporator.

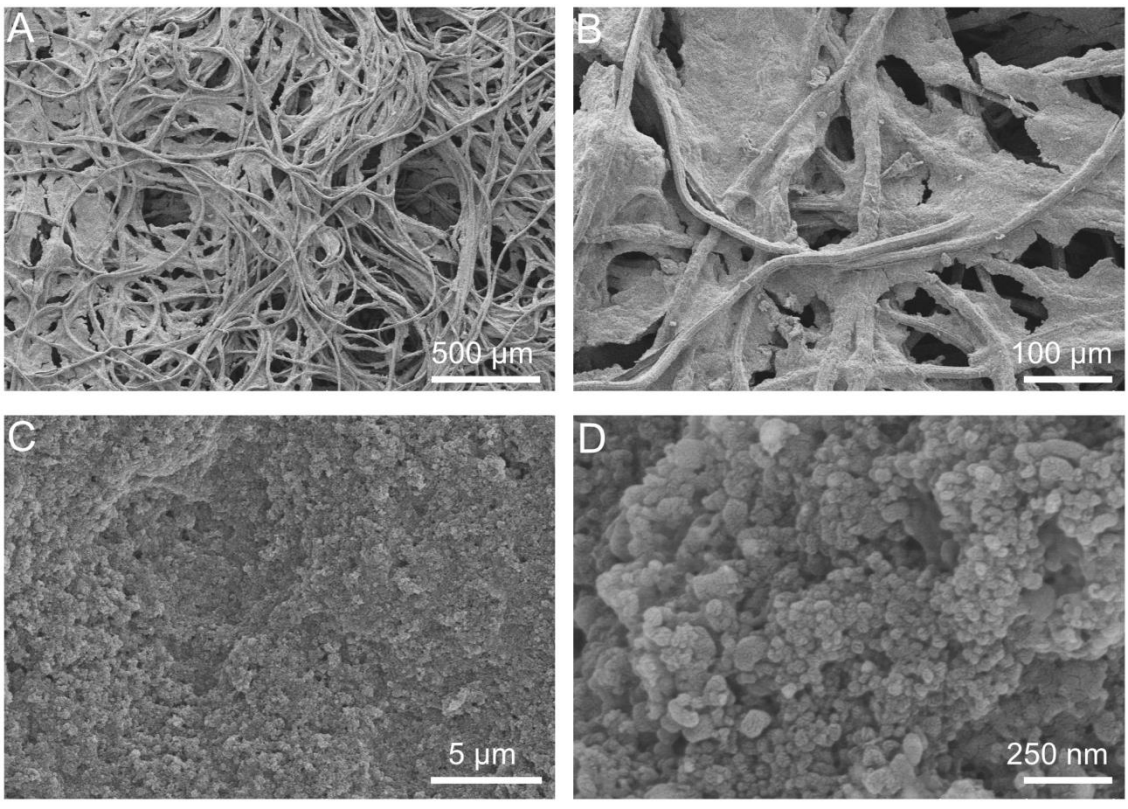

Supplementary Figure 17. (A-D) SEM images of $OCNT_{5\text{-}0.1\text{-}0}$ evaporator.

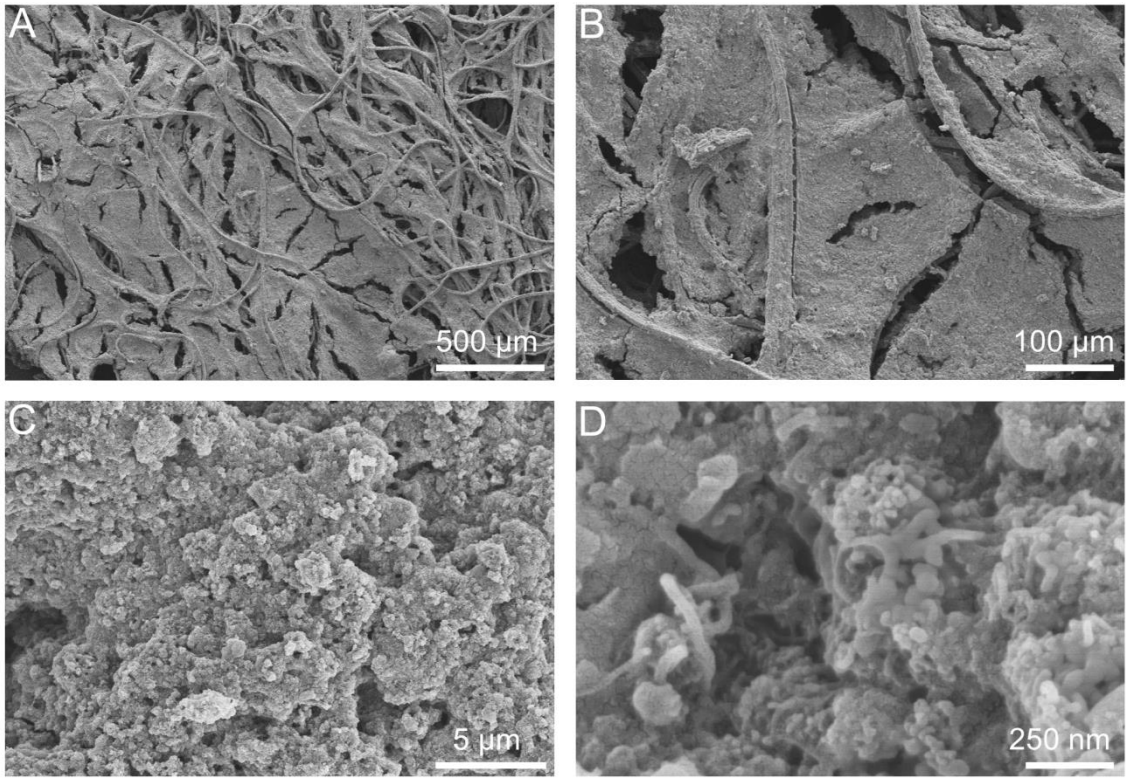

Supplementary Figure 18. (A-D) SEM images of $OCNT_{5\text{-}0\text{-}0.5}$ evaporator.

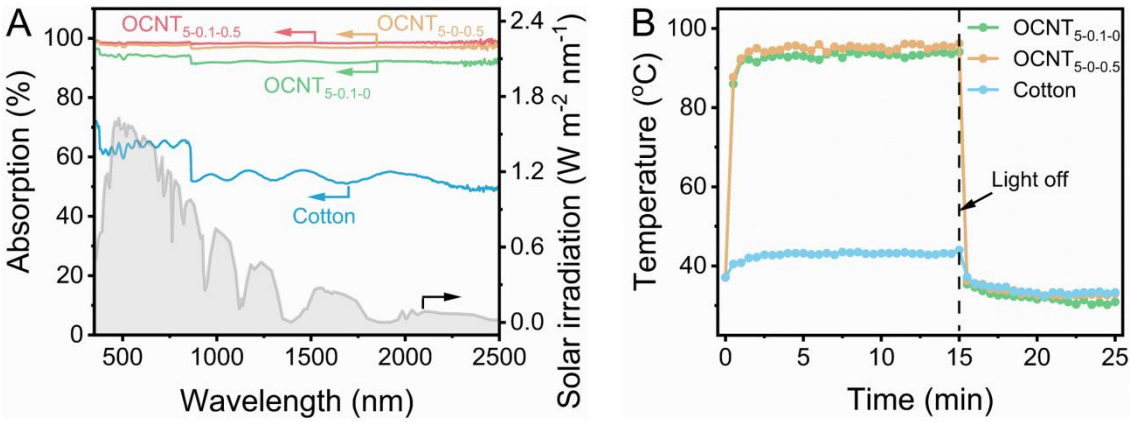

Supplementary Figure 19. (A) UV-Vis-NIR absorption spectra and (B) surface temperature curves of cotton and $OCNT_{x\text{-}y\text{-}z}$ evaporators.

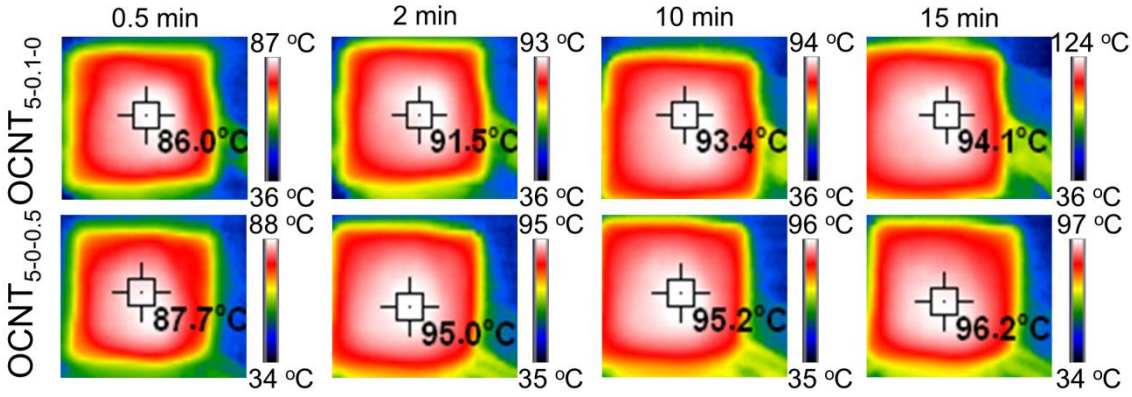

Supplementary Figure 20. Infrared images of $OCNT_{5\text{-}0.1\text{-}0}$ and $OCNT_{5\text{-}0\text{-}0.5}$ evaporators under 1 Sun irradiation.

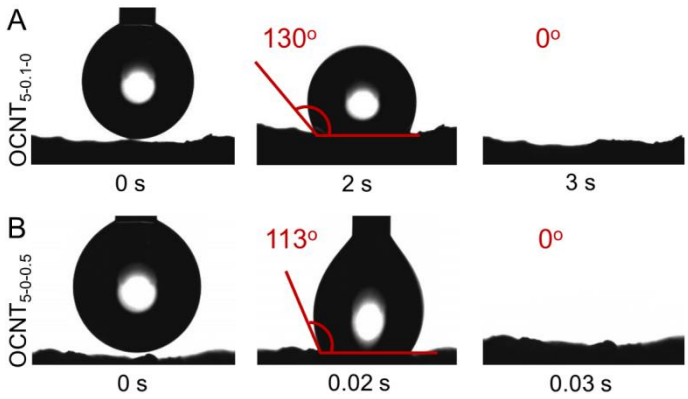

Supplementary Figure 21. Water contact angles of (A) $OCNT_{5\text{-}0.1\text{-}0}$ and (B) $OCNT_{5\text{-}0\text{-}0.5}$.

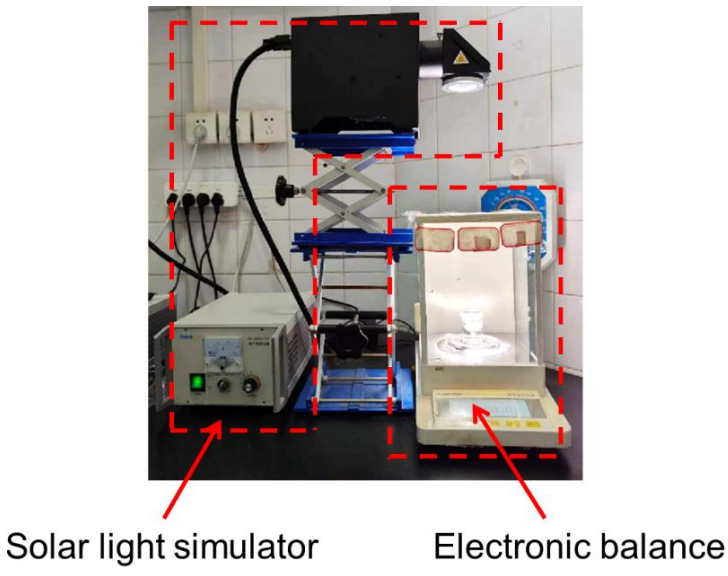

Supplementary Figure 22. Photograph of the interfacial solar evaporation system.

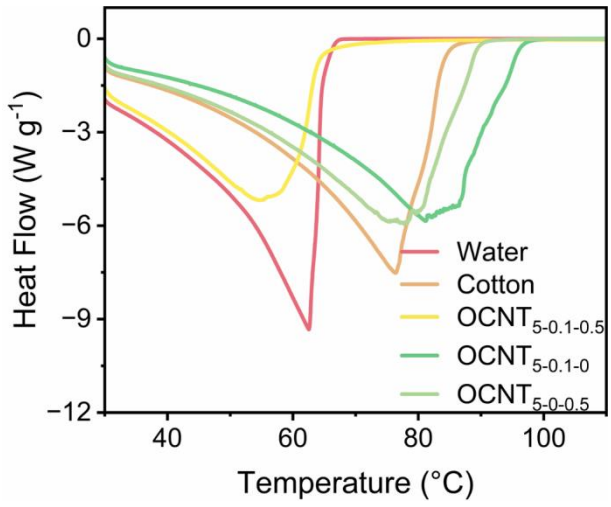

Supplementary Figure 23. DSC curves of water evaporation for different evaporators.

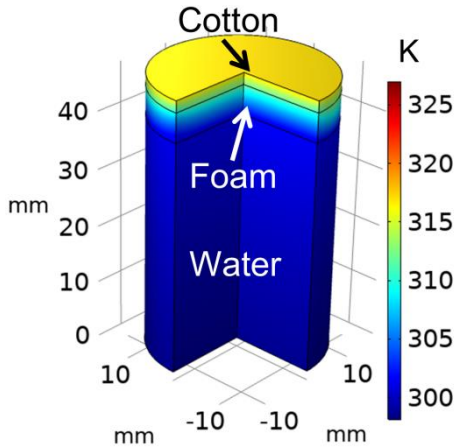

Supplementary Figure 24. COMSOL simulation of cotton evaporation system

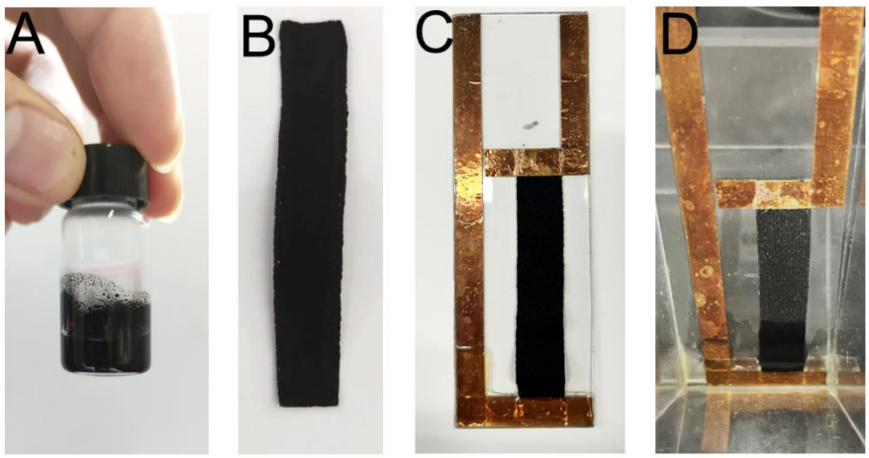

Supplementary Figure 25. (A-D) Pictures showing the preparation process of the $OCNT_{x\text{-}y\text{-}z}$ device.

Note: Firstly, $OCNT_{x\text{-}y\text{-}z}$ (50 mg) was added to the gelatin solution (2 wt%, 1120 μL) and

stirred overnight at room temperature (12 h, 400 rpm, step A). Then, the mixture was spread onto cotton cloth (1.5 × 10 cm^2) and dried in the atmosphere (step B). $OCNT_{x\text{-}y\text{-}z}$ evaporators were prepared after soaking and crosslinking with glutaraldehyde aqueous solution (5 wt%) for 5 h. Next, the $OCNT_{x\text{-}y\text{-}z}$ evaporator was placed on the PET substrate and fixed with conductive adhesive as electrodes (step C). Finally, the connecting part of the electrode and the device was coated with epoxy resin. After drying at room temperature for 15 min, the encapsulated evaporation device was obtained.

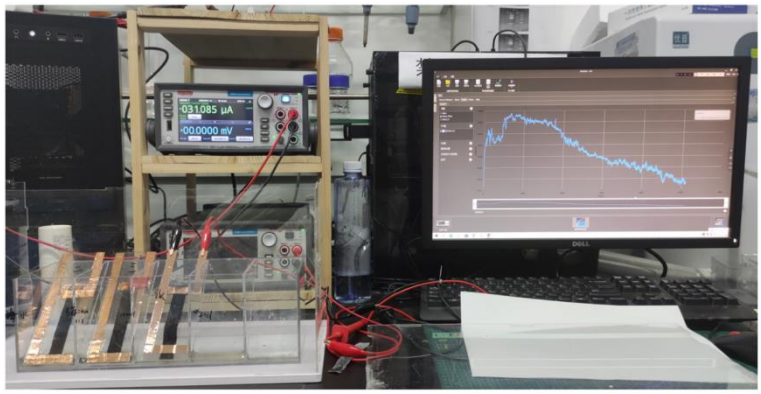

Supplementary Figure 26. Overall diagram of water-evaporation power generation in real time.

Note: The connected wire power generation device is being tested, and others are spare evaporation devices.

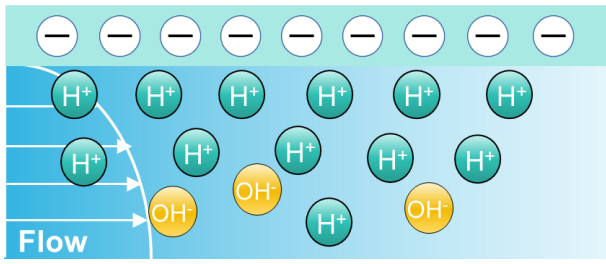

Supplementary Figure 27. Surface charge distribution model of $OCNT_{5\text{-}0.1\text{-}0.5}$ in pure water.

Note: Oxygen-containing functional groups on $OCNT_{5\text{-}0.1\text{-}0.5}$ surface (such as -COOH) can partially dissociate in water and generate negatively charged sites. Through electrostatic interaction, H_3O^+ accumulates near the $OCNT_{5\text{-}0.1\text{-}0.5}$ surface and forms an

electrical double layer, whereas OH^- is repelled from the negatively charged interface. Under water evaporation-induced flow, H_3O^+ and OH^- migrate directionally at different rates, leading to the separation of ionic charge and the generation of streaming potential.

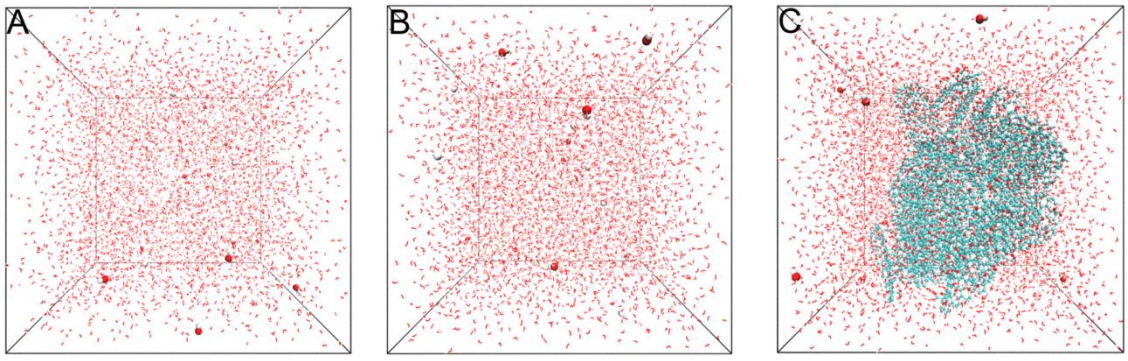

Supplementary Figure 28. Snapshot of MD simulations of (A) initial-state and (B) end-state result with pure water, and (C) end-state result with $OCNT_{5\text{-}0.1\text{-}0.5}$, H^+, OH^-, and pure water.

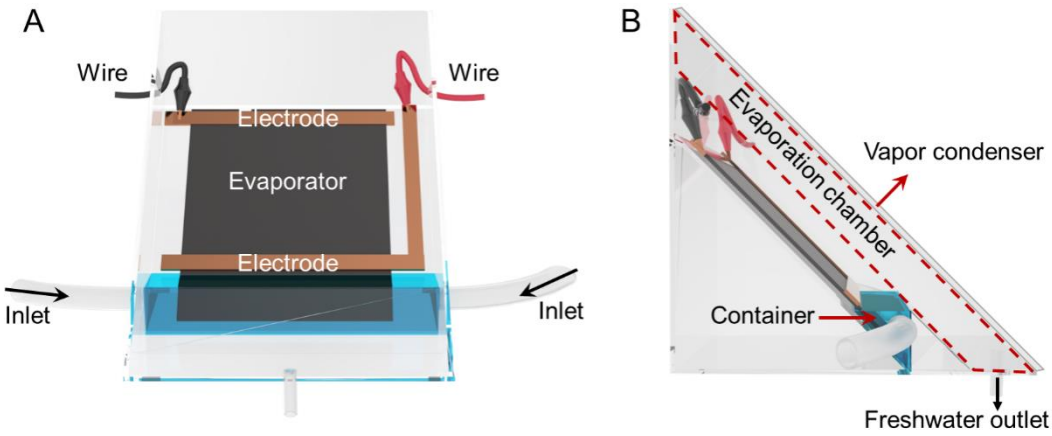

Supplementary Figure 29. Scheme of the practical solar-evaporation device from (A) front view and (B) left view.

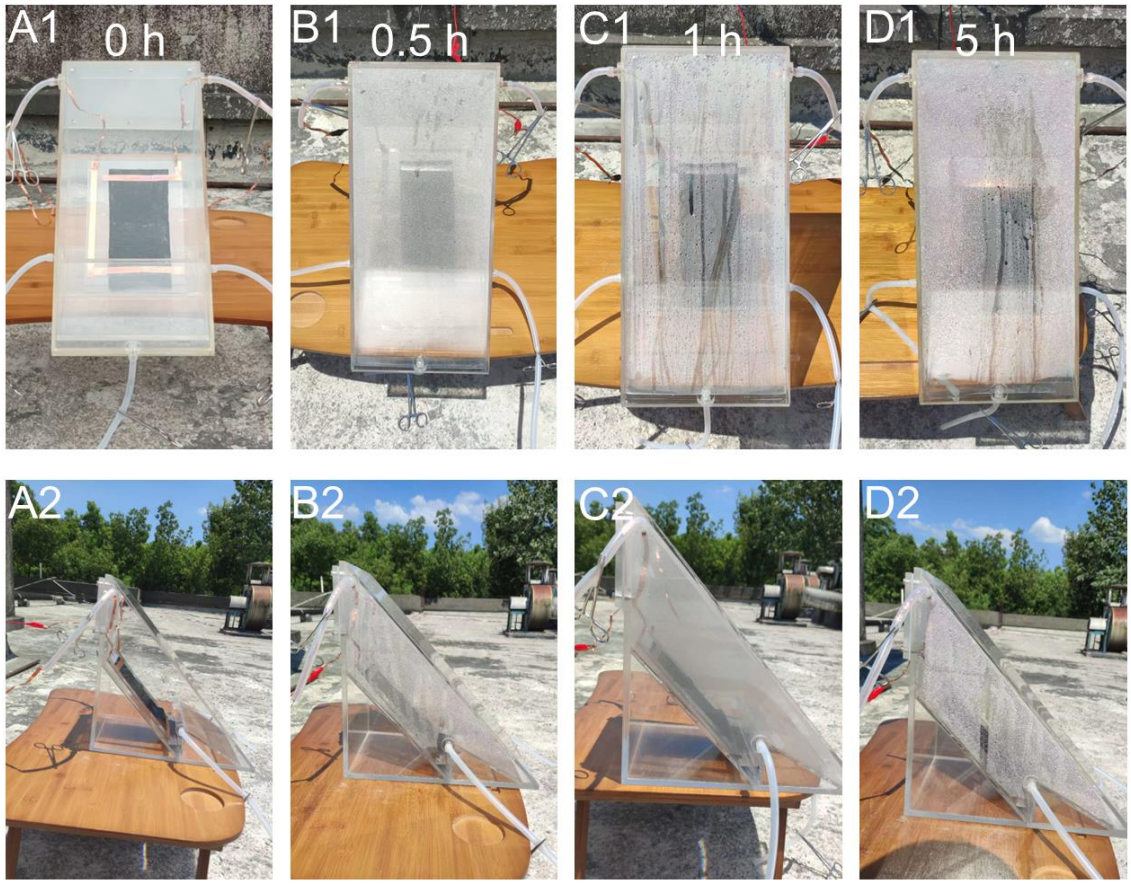

Supplementary Figure 30. Photographs of water evaporation and power generation in an outdoor experiment at different time: (A1 and A2) 0 h, (B1 and B2) 0.5 h, (C1 and C2) 1 h, and (D1 and D2) 5 h.

Supplementary Figure 31. Photograph for the series and parallel experiments of ten power generation devices to charge capacitors.

Supplementary Table 1. The material quantities added for each catalyst composition.

Catalysts	$Ni(NO_3)_2 \cdot 6H_2O$ (g)	$(NH_4)_6Mo_7O_{24} \cdot 4H_2O$ (g)	$Mg(NO_3)_2 \cdot 6H_2O$ (g)	PEG-200 (g)
$Ni_5Mo_{0.1}Mg_{0.5}$	30.00	0.36	2.64	10.00
$Ni_5Mo_0Mg_{0.5}$	30.00	0	2.64	10.00
$Ni_5Mo_{0.05}Mg_{0.5}$	30.00	0.18	2.64	10.00
$Ni_5Mo_{0.5}Mg_{0.5}$	30.00	1.82	2.64	10.00
$Ni_5Mo_1Mg_{0.5}$	30.00	3.64	2.64	10.00
$Ni_5Mo_{0.1}Mg_0$	30.00	0.36	0	10.00
$Ni_5Mo_{0.1}Mg_{0.1}$	30.00	0.36	0.53	10.00
$Ni_5Mo_{0.1}Mg_1$	30.00	0.36	5.29	10.00
$Ni_5Mo_{0.1}Mg_2$	30.00	0.36	10.58	10.00

Supplementary Table 2. The material quantities added in $OCNT_{x\text{-}y\text{-}z}$ evaporators with different sizes.

Application	Area (cm^2)	$OCNT_{x\text{-}y\text{-}z}$ (mg)	2% gelatin (μL)	Corresponding Figures
Scale-up preparation	176.62	588	13202	Figure 4A
Water evaporation indoor	6.15	20.5	460	Figure 5A, Supplementary Figure 22
Power generated indoor	15	50	1120	Figure 6A, Supplementary Figure 25
Practical experiment	200	666	14949	Figure 7A, Supplementary Figure 30

Supplementary Table 3. Comparison of the interfacial solar steam generation performance of $OCNT_{5\text{-}0.1\text{-}0.5}$ evaporator with recently reported photothermal materials under 1 kW m^{-2} irradiation.

Entry	Photothermal materials	Evaporation flux (kg m^{-2} h^{-1})	Efficiency (%)	Reference in Supplementary Material
1	$OCNT_{5\text{-}0.1\text{-}0.5}$ evaporator	2.73	95.4	This work
2	CCN evaporator	2.70	98.6	[1]
3	PCC-800	2.49	90.8	[2]
4	Bi-MOF	2.16	87.5	[3]

5	CPB-PVA-5	3.50	98.5	[4]
6	ZCP-20	2.48	67.1	[5]
7	MnO/C-600 membrane	2.38	98.4	[6]
8	CSL-C@MXene-20 mg	2.35	88.2	[7]
9	CMSx aerogel	2.34	91.7	[8]
10	Plasmonic wooden flower	2.08	97	[9]
11	Sunflower stalk pith	1.9	98.8	[10]
12	Highly hydratable hydrogel network	3.18	99	[11]
13	PPy sponge	1.89	85.6	[12]
14	GCP-20	1.87	79.2	[13]
15	CDW@MOF	1.81	89	[14]
16	FR@EC/rGO	1.83	94.2	[15]
17	TPA-SBTQ	1.337	92	[16]
18	Co-MOF/CNT membrane	2.25	89.1	[17]

Supplementary Table 4. Summary of the enthalpy values measured from the dark experiment and DSC measurement.

Enthalpy (kJ g^{-1})	Pure water	Cotton	$OCNT_{5\text{-}0.1\text{-}0.5}$	$OCNT_{5\text{-}0.1\text{-}0}$	$OCNT_{5\text{-}0\text{-}0.5}$
Dark experiment	2.434	2.347	1.686	1.995	1.915
DSC measurement	2.301	2.043	1.538	1.932	1.896

Supplementary Table 5. Comparison of voltage and evaporation flux of $OCNT_{5\text{-}0.1\text{-}0.5}$ evaporator/generator with some reported evaporators/generators.

Entry	Materials	Voltage (mV)	Evaporation flux ($kg\ m^{-2}\ h^{-1}$)	Reference in SI
1	$OCNT_{5\text{-}0.1\text{-}0.5}$	221	2.73	This work
2	CB/PVDF	320	1.44	[18]
3	Chiber@CNT/rGO-60%	260	2.1	[19]
4	Multiwalled CNT modified wood	250	1.19	[20]
5	PCP-600 device	212	2.74	[21]
6	PCC-800	201	2.49	[2]
7	MC30	168	2.24	[22]
8	Carbon cloth	141	1.48	[23]
9	Nb_4N_5 nanosheet	135	2.30	[24]
10	Carbon fiber	117	1.33	[25]
11	CNTs/carbon fiber foam	105	1.67	[26]
12	CNTP	100	1.28	[27]
13	$MoS_{2\text{-}x}$ NSAs	98.2	1.32	[28]
14	In_2O_3/TiO_2	80	1.51	[29]
15	MXene nanosheet	120	3.3	[30]
16	CNTs/cellulose sponge	60	1.20	[31]

Supplementary Note 1

Calculation of evaporation flux and conversion efficiency

The interfacial solar vapor generation system consisted of a solar light simulator (PLS-SXE300E), a UV reflection filter, an electronic balance (JA2003), and an infrared camera (DMI220). The surrounding temperature and relative humidity were approximately 25 ℃ and 33%, respectively. The infrared camera was used to collect surface temperature and thermal distribution of evaporators. Evaporation flux (m, kg m^{-2} h^{-1}) and conversion efficiency (η, %) of the evaporator were calculated through Equations S1 and S2, respectively,

$$m = \Delta m / (S \times t) \quad \text{(S1)}$$

$$\eta = m' \times h_{LV} / (3600 \times P_{in}) \quad \text{(S2)}$$

where Δm stands for the water mass loss in 1 h (kg), S represents the lighting area of the evaporator (6.15×10^{-4} m^2), t refers to the irradiation time (1 h), m' presents the evaporation flux that subtracts the darkroom evaporation flux, h_{LV} represents the water evaporation enthalpy (kJ kg^{-1}), and P_{in} stands for the illumination intensity (1 kW m^{-2}).

Supplementary Note 2

Characterization

Scanning electron microscopy (SEM, Hitachi, SU8010, Japan) was used to investigate the morphology of $OCNT_{5\text{-}0.1\text{-}0.5}$ and $OCNT_{5\text{-}0.1\text{-}0.5}$ evaporator. The crystal structure was analyzed by X-ray diffraction (XRD, Rigaku, SmartLab-SE, Japan). The metallic oxide of catalysts and the crystal structure of carbon materials were analyzed by Raman spectroscopy (HORIBA Jobin Yvon, LabRAM HR800, Japan). The thermal stability of $Ni_5Mo_{0.1}Mg_{0.5}$ and $OCNT_{5\text{-}0.1\text{-}0.5}$ was measured by thermal gravimetric analysis (TGA, Perkin Elmer, Pyris1 TGA, China). H_2-temperature programmed reduction (H_2-TPR, JWGB, AMI-300, China) analysis was conducted with a temperature ramp of 10 °C min^{-1} under a gas flow consisting of a mixture of hydrogen and argon (H_2:Ar = 10:90, 30 mL min^{-1}). Before the TPR evaluation, catalysts were pretreated with Ar gas at 200 °C for 1 h. During the reduction process, the amount of H_2 consumption was measured using a thermal conductivity detector (TCD). CO_2-temperature programmed desorption (CO_2-

TPD) experiments were performed on a multifunction chemisorption analyzer (JWGB, AMI-300, China). A mixture of CO_2 and He (CO_2:He = 10:90) was selected as the gas flow. The CO_2 TPD was carried out under an Ar flow of 30 mL min^{-1} with a heating speed of 10 °C min^{-1}; the liberated CO_2 was monitored by TCD signals. The specific surface area and pore structure of $OCNT_{5\text{-}0.1\text{-}0.5}$ were measured by the surface analyzer (Micromeritics, ASAP 2460, America). The density functional theory (DFT) model or Barret-Joyner-Halenda (BJH) model was used to determine the pore size distribution. The functional group of $OCNT_{5\text{-}0.1\text{-}0.5}$ was analyzed by Fourier-transform infrared spectroscopy (FT-IR, BRUKER, Vertex 80, Germany) and X-ray photoelectron spectroscopy (XPS, Thermo Fisher, ESCALAB 250XI, America). Light absorption was tested via a UV-Vis-NIR spectrophotometer (Perkin Elmer, Lambda 750 S, China) within the spectral range of 300-2500 cm^{-1}. The water contact angle of the OCNT evaporator was measured by micro-optical contact angle measurement instrument (Dataphysics, OCA15EC, Germany). Thermal conductivity was tested by a thermal conductivity analyzer (Hot Disk AB, TPS 2500, Sweden). The evaporation enthalpy of evaporators was analyzed by a differential scanning calorimeter (DSC, Perkin Elmer, Diamond DSC, China). The surface temperature distribution was examined using the COMSOL Multiphysics 5.6 software. Open-circuit voltage and short-circuit current were tested by a Digital SourceMeter (Beijing JKZC Technology Development Co., Ltd., Keithley 2450, China). Zeta potential was measured by using BeNano180Zeta (China).

Supplementary Note 3

Calculation of water evaporation enthalpy

The energy for water to evaporate in the dark is gained from the environment, which is therefore the same for different evaporators.

Considering theoretical evaporation enthalpy of liquid water is ca. 2.434 kJ g^{-1}. Then enthalpy values are obtained as follows,

$$U_{in}=E_{aque}m_g=E_0m_0 \quad \text{(S3)}$$

where U_{in} is the total energy absorbed from the environment per hour; E_0 and m_0

refer to the water vaporization enthalpy (2.43 kJ g^{-1}) and the water mass loss (g) of pure water without evaporators in the dark, respectively; E_{aque} is the equivalent evaporation enthalpy of the corresponding system (kJ g^{-1}), and m_g means the corresponding water mass change.

The mass loss of pure water, cotton, $OCNT_{5\text{-}0.1\text{-}0.5}$, $OCNT_{5\text{-}0.1\text{-}0}$, and $OCNT_{5\text{-}0\text{-}0.5}$ evaporators in the dark are 295, 306, 426, 360, and 375 mg, respectively. Therefore, the water evaporation enthalpy of cotton cloth, $OCNT_{5\text{-}0.1\text{-}0.5}$, $OCNT_{5\text{-}0.1\text{-}0}$, and $OCNT_{5\text{-}0\text{-}0.5}$ are 2.347, 1.686, 1.995 and 1.915 kJ g^{-1}, respectively, which is reduced by 3.5%, 30.7%, 18% and 21.3%, respectively, in comparison to pure water (2.434 kJ g^{-1}).

Supplementary Note 4

COMSOL simulation

The simulated 3D models were established based on the actual $OCNT_{5\text{-}0.1\text{-}0.5}$ membrane evaporation system, which mainly consisted of $OCNT_{5\text{-}0.1\text{-}0.5}$ membrane, PS foam, and bulk water. The upper hollow cylinder with 2 mm in height and 15 mm in radius was simulated to the membrane evaporator, the middle core cylinder with 3 mm in height and 15 mm in radius was simulated to the floating PS foam, and the remainder of a whole cylinder with 40 mm in height and 15 mm in radius was simulated to the bulk water. Subsequently, the temperature distribution was described as the following equations,

$$E_{in}=\rho C_P \frac{\partial T}{\partial t}+\rho C_P u\cdot\nabla T+\nabla q \quad \text{(S4)}$$

$$q=-k\nabla T \quad \text{(S5)}$$

where E_{in} is the thermal energy input from the solar irradiation; T (x, t) refers to the local temperature; x and t are the space vector and time, respectively; ρ, C_P and k are the mass density, specific thermal capacity, and thermal conductivity of the evaporator, respectively; u is the fluid flow speed of the aqueous medium.

The theoretical simulation was performed by COMSOL Multiphysics 5.6 under the steady-state analysis mode. The environment temperature was set to 298.15 K, and the heat convection between the upper surface of evaporator and air was corrected by Newton's law of cooling. The thermal conductivity, density, and specific thermal

capacity of cotton cloth are 0.0674 W m^{-1} K^{-1}, 67 kg m^{-3}, and 4025.43 J kg^{-1} K^{-1}, respectively. The thermal conductivity, density, and specific thermal capacity of $OCNT_{5\text{-}0.1\text{-}0.5}$ are 0.0752 W m^{-1} K^{-1}, 101 kg m^{-3}, and 2658.27 J kg^{-1} K^{-1}, respectively. The thermal conductivity, density, and specific thermal capacity of PS foam are 0.03 W m^{-1} K^{-1}, 30 kg m^{-3}, and 1300 J kg^{-1} K^{-1}, respectively.

Supplementary Note 5

Analyses of heat loss

Normally, the heat loss of water evaporation process includes radiation, convection, and conduction. The calculating details of heat loss are shown as follows,

(1) Heat radiation

The heat radiation loss was calculated by the Stefan-Boltzmann equation,

$$\emptyset=\varepsilon A\sigma(T_1^4-T_2^4) \quad \text{(S6)}$$

where $\emptyset$ represents the heat flux, ε is the emissivity, and the emissivity in the water evaporation processes is supposed to have a maximum emissivity of 1. A is the effective evaporation surface area (6.16×10^{-4} m^2). σ is the Stefan-Boltzmann constant (the value is 5.67×10^{-8} W m^{-2} K^{-4}). T_1 is the surface temperature of the materials after stable steam generation under one-sun illumination (ca. 55.6 °C, 328.75 K), and T_2 is the ambient temperature upward of the absorber (ca. 39.4 °C, 312.55 K). Then using the following equation to calculate the radiation loss,

$$\eta_{rad}=\emptyset/P_{in} \quad \text{(S7)}$$

Therefore, the calculated heat radiation loss of the $OCNT_{5\text{-}0.1\text{-}0.5}$ evaporator is 7.5%.

(2) Heat convection

The convective heat loss is defined by Newton's law of cooling as shown below,

$$Q=\mathrm{h}A\Delta T \quad \text{(S8)}$$

where Q is the convection heat flux, h represents the convection heat transfer coefficient, which is approximately 5 W m^{-2} K^{-1}. ΔT is the difference between the surface temperature of $OCNT_{5\text{-}0.1\text{-}0.5}$ evaporator and the ambient temperature upward the absorber. Consequently, the connection heat loss of the $OCNT_{5\text{-}0.1\text{-}0.5}$ evaporator was calculated

through Equation S8, and the value is 4.9%.

(3) Heat conduction

$$Q=Cm\Delta T \quad \text{(S9)}$$

where Q is the heat energy, C presents the specific heat capacity of water (4.2 kJ K^{-1} kg^{-1}), and m denotes the weight of water (g). ΔT is the increased temperature of water. In this work, m = 35 g, ΔT = 0.5 K, Consequently, according to Equation S9, the calculated conduction heat loss of the $OCNT_{5\text{-}0.1\text{-}0.5}$ evaporator is ca. 3.3%.

Therefore, the heat loss of the $OCNT_{5\text{-}0.1\text{-}0.5}$ evaporator in the water evaporation is ca. 15.7%.

Supplementary Note 6

Theoretical calculation

The size of $OCNT_{5\text{-}0.1\text{-}0.5}$ synthesized in the experiment is too large, and single-side graphene oxide (GO) fragments are used to simulate $OCNT_{5\text{-}0.1\text{-}0.5}$ in the simulation calculation. The partial charge of GO with different oxygen content was calculated using Gaussian 16 code[32] and the 6-311g (d,p) basis functions were applied[33]. The OPLSS-AA force field[34] and Auxiliary Tools of Force Field (AuToFF) were used to parametrize all atoms, such as bond parameters, angle parameters, and dihedral angles.

The interactions of different graphene oxide with H^+ and OH^- were studied by molecular dynamics (MD) simulation. In system 1, 30 GO molecules, 10 H^+, 10 OH^- and 5560 water molecules were randomly inserted into a cube box with a side length of 7.0 nm. The model of water molecule is TIP_3P[35]. The MD simulations were performed in the GROMACS 2021 software package[36-38]. The steepest descent method was applied to minimize the initial energy for each system with a force tolerance of 1 kJ mol^{-1} nm^{-1} and a maximum step size of 0.002 ps before MD calculations[39]. In all the three directions, periodic boundary conditions were imposed. Leapfrog algorithm was used to integrate the Newtonian equation of motion[39]. The MD simulation was processed in an NPT ensemble and the simulation time is 20 ns. In system 2, 10 H^+, 10 OH^- and 5560 water molecules were added into the simulated system. Other operation steps are the same as

the system 1.

In NPT simulations, the pressure was maintained at 1 bar by the Berendsen barostat in an isotropic manner[40]. The temperature was maintained by the V-rescale thermostat at 298.15 K. The LINCS algorithm[41] was performed for constrain bond lengths of hydrogen atoms. A cutoff of 1.0 nm was employed to calculate the short-range van der Waals interactions and the electrostatic interactions[42].

REFERENCES

1. Liu, J.; Fan, Z.; Liu, H.; et al. Upcycling of waste poly(lactic acid) into crumped carbon nanosheet towards high-performance interfacial solar-driven evaporation. *J. Environ. Chem. Eng.* **2024**, *12*, 112363, DOI: 10.1016/j.jece.2024.112363.
2. Chen, B.; Ren, J.; Song, Y.; et al. Upcycling waste poly(ethylene terephthalate) into a porous carbon cuboid through a MOF-derived carbonization strategy for interfacial solar-driven water–thermoelectricity cogeneration. *ACS Sustainable Chem. Eng.* **2022**, *10*, 16427-16439, DOI: 10.1021/acssuschemeng.2c05722.
3. Fan, Z.; Liu, J.; Liu, H.; et al. Synergism of solar-driven interfacial evaporation and photo-fenton Cr(VI) reduction by sustainable Bi-MOF-based evaporator from waste polyester. *J. Energy Chem.* **2024**, *94*, 527-540, DOI: 10.1016/j.jechem.2024.03.011.
4. Ge, Y.; Wang, L.; Su, Z.; et al. Efficient solar-driven interfacial water evaporator using hydrogel modified carbon-based biomass with abundant microchannels. *Small* **2024**, *20*, 2309780, DOI: 10.1002/smll.202309780.
5. Zhu, Y.; Lan, H.; He, P.; et al. Composite membranes based on self-crosslinking polyelectrolyte-wrapped ZIF-8/CNT nanoparticles for solar steam evaporation. *Mater. Adv.* **2023**, *4*, 1628-1636, DOI: 10.1039/d3ma00075c.
6. Fan, Z.; Ren, J.; Bai, H.; et al. Shape-controlled fabrication of MnO/C hybrid nanoparticle from waste polyester for solar evaporation and thermoelectricity generation. *Chem. Eng. J.* **2023**, *451*, 138534, DOI: 10.1016/j.cej.2022.138534.
7. Zhang, G.; Zhang, Y.; Jiang, J. Robust and multifunctional MXene/rGO composite aerogels toward highly efficient solar-driven interfacial evaporation and wastewater treatment. *Sep. Purif. Technol.* **2024**, *347*, 127588, DOI: 10.1016/j.seppur.2024.127588.
8. Zhang, C.; Wang, Y.; Liu, Q.; et al. Biomimetic polyaryl ether-based aerogels for efficient interfacial solar water vapor generation. *Chem. Eng. J.* **2024**, *489*, 151247, DOI: 10.1016/j.cej.2024.151247.
9. Chen, S.; Sun, Z.; Xiang, W.; et al. Plasmonic wooden flower for highly efficient solar vapor generation. *Nano Energy* **2020**, *76*, 104998, DOI: 10.1016/j.nanoen.2020.104998.
10. Su, X.; Hao, D.; Sun, M.; et al. Nature sunflower stalk pith with zwitterionic

hydrogel coating for highly efficient and sustainable solar evaporation. *Adv. Funct. Mater.* **2022**, *32*, 2108135, DOI: 10.1002/adfm.202108135.

11. Zou, H.; Meng, X.; Zhao, X.; Qiu, J. Hofmeister effect-enhanced hydration chemistry of hydrogel for high-efficiency solar-driven interfacial desalination. *Adv. Mater.* **2023**, *35*, 2207262, DOI: 10.1002/adma.202207262.
12. Yu, Z.; Su, Y.; Gu, R.; Wu, W.; Li, Y.; Cheng, S. Micro–nano water film enabled high-performance interfacial solar evaporation. *Nano-Micro Lett.* **2023**, *15*, 214, DOI: 10.1007/s40820-023-01191-6.
13. Han, J.; Dong, Z.; Hao, L.; Gong, J.; Zhao, Q. Poly(ionic liquid)-crosslinked graphene oxide/carbon nanotube membranes as efficient solar steam generators. *Green Energy Environ.* **2023**, *8*, 151-162, DOI: 10.1016/j.gee.2021.03.010.
14. Jing, S.; Ji, Q.; Wang, A.; et al. Fe-based metal organic frameworks decorated wood for efficient solar-driven interfacial water evaporation. *Appl. Therm. Eng.* **2024**, *244*, 122629, DOI: 10.1016/j.applthermaleng.2024.122629.
15. Sui, Z.; Xue, X.; Wang, Q.; et al. Facile fabrication of 3D janus foams of electrospun cellulose nanofibers/rGO for high efficiency solar interface evaporation. *Carbohydr. Polym.* **2024**, *331*, 121859, DOI: 10.1016/j.carbpol.2024.121859.
16. Wang, L.; Wang, H.; Yu, S.; et al. Manipulating molecular motion of [1,2,5]Thiadiazolo[3,4-g]Quinoxaline-6,7-Dicarboxylate small molecules for highly efficient solar-thermal water evaporation and thermoelectric power generation. *Adv. Funct. Mater.* **2024**, *34*, 2315762, DOI: 10.1002/adfm.202315762.
17. Bai, H.; He, P.; Hao, L.; et al. Waste-treating-waste: Upcycling discarded polyester into metal-organic framework nanorod for synergistic interfacial solar evaporation and sulfate-based advanced oxidation process. *Chem. Eng. J.* **2023**, *456*, 140994, DOI: 10.1016/j.cej.2022.140994.
18. Huang, J.; Pereira, V.; Wang, C.; Li, H.; Lee, H.K.; Han, J. A dual-functional device based on CB/PVDF@BFP for solar-driven water purification and water-induced electricity generation. *J. Mater. Chem. A* **2023**, *11*, 8110-8118, DOI: 10.1039/d3ta00032j.
19. Wu, Y.; Ma, J.; Zang, S.; et al. Multifunctional composite membranes for interfacial solar steam and electricity generation. *Chem. Eng. J.* **2023**, *472*, 144600, DOI: 10.1016/j.cej.2023.144600.
20. Ding, Y.; Li, S.; Tian, J.; et al. CNTs/Wood composite nanogenerator for producing both steam and electricity. *ACS Appl. Electron. Mater.* **2021**, *3*, 5287-5295, DOI: 10.1021/acsaelm.1c00796.
21. Liu, H.; Liu, L.; Fan, Z.; et al. Transforming waste polyester into porous carbon polyhedron for interfacial solar steam and hydrovoltaic electricity co-generation. *Chem. Eng. J.* **2024**, *485*, 149690, DOI: 10.1016/j.cej.2024.149690.
22. Ren, J.; Ding, Y.; Gong, J.; Qu, J.; Niu, R. Simultaneous solar-driven steam and electricity generation by cost-effective, easy scale-up MnO_2-based flexible membranes. *Energy Environ. Mater.* **2023**, *6*, e12376, DOI: 10.1002/eem2.12376.
23. Xu, Y.; Guo, Z.; Wang, J.; et al. Harvesting solar energy by flowerlike carbon

cloth nanocomposites for simultaneous generation of clean water and electricity. *ACS Appl. Mater. Interfaces* **2021**, *13*, 27129-27139, DOI: 10.1021/acsami.1c07091.

24. Wang, L.; Ma, Y.; Yang, G.; et al. Asymmetric solar evaporator with salt-resistance capability for freshwater and energy generation. *Chem. Eng. J.* **2023**, *472*, 144761, DOI: 10.1016/j.cej.2023.144761.
25. Wu, D.; Liang, J.; Zhang, D.; Zhang, C.; Zhu, H. Solar evaporation and electricity generation of porous carbonaceous membrane prepared by electrospinning and carbonization. *Sol. Energy Mater. Sol. Cells* **2020**, *215*, 110591, DOI: 10.1016/j.solmat.2020.110591.
26. Zhang, F.; Li, Y.; Cai, H.; Liu, Q.; Tong, G. Processing nanocellulose foam into high-performance membranes for harvesting energy from nature. *Carbohydr. Polym.* **2020**, *241*, 116253, DOI: 10.1016/j.carbpol.2020.116253.
27. Duan, Y.; Weng, M.; Zhang, W.; Qian, Y.; Luo, Z.; Chen, L. Multi-functional carbon nanotube paper for solar water evaporation combined with electricity generation and storage. *Energy Convers. Manage.* **2021**, *241*, 114306, DOI: 10.1016/j.enconman.2021.114306.
28. Yuan, B.; Yang, L.; Yang, H.; et al. Flexible vacancy-mediated MoS_{2-x} nanosheet arrays for solar-driven interfacial water evaporation, photothermal-enhanced photodegradation, and thermoelectric generation. *Energy Convers. Manage.* **2022**, *252*, 115070, DOI: 10.1016/j.enconman.2021.115070.
29. Xiang, P.; Tang, C.; Ma, K.; Li, X. Defects in In_2O_3/TiO_2 composite boosting photothermal conversion for water purification and electricity generation. *Sol. Energy Mater. Sol. Cells* **2024**, *268*, 112750, DOI: 10.1016/j.solmat.2024.112750.
30. Che, X.; Zhang, W.; Long, L.; et al. Mildly peeling off and encapsulating large MXene nanosheets with rigid biologic fibrils for synchronization of solar evaporation and energy harvest. *ACS Nano* **2022**, *16*, 8881-8890, DOI: 10.1021/acsnano.1c10836.
31. Zhu, L.; Ding, T.; Gao, M.; Peh, C.K.N.; Ho, G.W. Shape conformal and thermal insulative organic solar absorber sponge for photothermal water evaporation and thermoelectric power generation. *Adv. Energy Mater.* **2019**, *9*, 1900250, DOI: 10.1002/aenm.201900250.
32. Frisch, M.J.; Trucks, G.W.; Schlegel, H.B.; et al. *Gaussian 16 Rev. C.01*, Wallingford, CT, 2016.
33. Petersson, G.A.; Al-Laham, M.A. A complete basis set model chemistry. II. open-shell systems and the total energies of the first-row atoms. *J. Chem. Phys.* **1991**, *94*, 6081-6090, DOI: 10.1063/1.460447.
34. Jorgensen, W.L.; Maxwell, D.S.; Tirado-Rives, J. Development and testing of the OPLS all-atom force field on conformational energetics and properties of organic liquids. *J. Am. Chem. Soc.* **1996**, *118*, 11225-11236, DOI: 10.1021/ja9621760.
35. Jorgensen, W.L.; Chandrasekhar, J.; Madura, J.D.; Impey, R.W.; Klein, M.L. Comparison of simple potential functions for simulating liquid water. *J. Chem. Phys.* **1983**, *79*, 926-935, DOI: 10.1063/1.445869.
36. Van Der Spoel, D.; Lindahl, E.; Hess, B.; Groenhof, G.; Mark, A.E.; Berendsen,

H.J.C. GROMACS: Fast, flexible, and free. *J. Comput. Chem.* **2005**, *26*, 1701-1718, DOI: 10.1002/jcc.20291.

37. Abraham, M.J.; Murtola, T.; Schulz, R.; et al. GROMACS: High performance molecular simulations through multi-level parallelism from laptops to supercomputers. *SoftwareX* **2015**, *1-2*, 19-25, DOI: 10.1016/j.softx.2015.06.001.
38. Berendsen, H.J.C.; van der Spoel, D.; van Drunen, R. GROMACS: A message-passing parallel molecular dynamics implementation. *Comput. Phys. Commun.* **1995**, *91*, 43-56, DOI: 10.1016/0010-4655(95)00042-E.
39. Van Gunsteren, W.F.; Berendsen, H.J.C. A leap-frog algorithm for stochastic dynamics. *Mol. Simul.* **1988**, *1*, 173-185, DOI: 10.1080/08927028808080941.
40. Berendsen, H.J.C.; Postma, J.P.M.; van Gunsteren, W.F.; DiNola, A.; Haak, J.R. Molecular dynamics with coupling to an external bath. *J. Chem. Phys.* **1984**, *81*, 3684-3690, DOI: 10.1063/1.448118.
41. Hess, B.; Bekker, H.; Berendsen, H.J.C.; Fraaije, J.G.E.M. LINCS: A linear constraint solver for molecular simulations. *J. Comput. Chem.* **1997**, *18*, 1463-1472, DOI: 10.1002/(SICI)1096-987X(199709)18:12<1463::AID-JCC4>3.0.CO;2-H.
42. Darden, T.; York, D.; Pedersen, L. Particle mesh ewald: An N·log(N) method for ewald sums in large systems. *J. Chem. Phys.* **1993**, *98*, 10089-10092, DOI: 10.1063/1.464397.